Equilibrium Dynamics of Complex Fluids studied via X-ray Photon Correlation Spectroscopy at 8-ID at the APS

S. G. J. Mochrie
Department of Physics, Yale University, New Haven, CT 06520
E-mail: simon.mochrie@yale.edu

I Introduction

In these notes, I will present my own perspective concerning x-ray photon correlation spectroscopy (XPCS) and some illustrative XPCS measurements. Specifically, I will describe how to prepare coherent x-ray beams suitable for XPCS and measurements on a static aerogel sample that characterize the beam coherence, independent of any assumed coherence lengths. I will introduce XPCS in the context of measurements to characterize collective diffusion within concentrated colloidal suspensions. Then, I will discuss surface XPCS measurements aimed at determining the dynamics of capillary relaxations at the surface of a polymer thin film. Finally, I will mentioned new measurements to determine the dynamics of membranes within a so-called sponge phase, built out of block copolymers. All of these measurements were carried out at beamline 8-ID at the Advanced Photon Source (APS) at Argonne National Laboratory (ANL). It is important to realize, however, that there are XPCS programs ongoing both at the Advanced Light Source, and especially at the European Synchrotron Radiation Facility (ESRF).

The measurements that I will present were made possible by the efforts of a number of dedicated and talented people, who have created 8-ID and the XPCS capability there. In particular, I should like to thank Matt Borthwick, Peter Falus, Harold Gibson, Martin Holt, Dirk Lumma, Larry Lurio, Amit Malik, Suresh Narayanan, Jean-Francois Pelletier, Adrian Rühm, Alec Sandy, Brian Stephenson, Mark Sutton, and Gerry Swislow. Additionally, I should like to thank Alec Sandy, Larry Lurio, Amit Malik, Brian Stephenson and Mark Sutton for their collaboration on the aerogel speckle measurements[1], Larry Lurio, Dirk Lumma, Alec Sandy, Matt Borthwick, Peter Falus, Jean-Francois Pelletier, Mark Sutton, Lynne Regan, Amit Malik and Brian Stephenson for their colloaboration on the colloidal diffusion experiment[2,3], Hyunjung Kim, Adrian Rühm, Joydeep Basu, Jyotsana Lal, Larry Lurio, and Sunny Sinha for their collaboration on the experiment to study the dynammics of capillary modes on the surface of polymer films[4], and Peter Falus and Matt Borthwick for their collaboration on the experiment to study the dynamics of polymeric sponge phases. I am also grateful to the National Science Foundation (via DMR 9312548) and to the Department of Energy (via Grant DE-FG02-96ER45593) for funding the implementation of 8-ID, and to the NSF for supporting my recent XPCS-based research (via Grant DMR 0071755).

II XPCS: The big picture

At the beamline planning stage for third generation synchrotrons, it was widely recognized that one of the most exciting scientific opportunities offered by their then-unprecedented brilliance was the possibility of carrying out x-ray photon correlation spectroscopy (XPCS) experiments. Such experiments promise exciting new insights into dynamical phenomena in condensed matter, occurring on shorter length scales than can be reached in light scattering and longer time scales than can be reached with the neutron spin echo technique. Specifically, by illuminating the sample under study with a coherent beam, the PCS method reveals the characteristic times of the sample via autocorrelation of its (speckled) scattering pattern. The resultant intensity-intensity autocorrelation function $[g_2(Q,t)]$ is related to the intermediate scattering function (ISF) $[S(Q,t)]$ of the sample via

$$g_2(Q,t) = 1 + \beta[f(Q,t)]^2, \qquad (1)$$

where β is the optical contrast, $f(Q,t) = S(Q,t)/S(Q)$ is the normalized ISF, and $S(Q) = S(Q,0)$ is the static structure factor. On the theoretical side, there are books concerned with how to calculate $S(Q,t)$[5], which, for x-rays, is equivalent to the density-density correlation function. Suffice it to say here that XPCS provides a direct measurement of a key quantity of interest for any condensed matter system. The caveat, of course, is that only a certain range of length and time scales can be studied, and the trick is to find samples with interesting structure and dynamics within the accessible range.

PCS experiments with x-rays are much more challenging than those using lasers, first, because it is necessary to use a partially coherent x-ray beam, which contains far fewer photons than a laser beam, and, second, because the x-ray scattering cross-section is far smaller than for light scattering. As a result, the crucial aspect of an XPCS experiment is usually the signal-to-noise ratio (SNR). Thus, the source should be as brilliant as possible. The beamline optics should preserve the source brilliance. It is helpful to have a strongly scattering sample, which must be studied in a manner

that minimizes as far as possible x-ray sample damage. The detector should collect as many x-rays as possible over as wide an angular range as possible, with an angular resolution sufficiently fine to resolve or nearly resolve x-ray speckle, on a time scale commensurate with the sample's interesting dynamics. Beamline and synchrotron stability is essential to achieve clean results. Because XPCS is SNR-starved, enough beamtime must be allocated. Finally, when a CCD-base area detector is used, appropriate tools for data reduction, visualization and analysis must be created.

In spite of these challenges, there are several reasons that motivate the continued development of XPCS. First, it is already possible to carry out interesting experiments. I hope that the measurements I will describe below will support this claim. Second, although in the last several years, we have made important strides in our understanding of what is required of the optics for an XPCS beamline, in our time-resolved detection capabilities, and in our ability to analyse XPCS data, nevertheless, with further improvements in source brilliance, beamline optics and detectors, there will be considerable further gains in the XPCS SNR. In turn, these increased XPCS capabilities and the development of a sufficiently user-friendly XPCS environment will grow an XPCS user community, in part, from the optical PCS community, and, in part, from the SAXS/SANS/scattering communities. For these reasons, together with burgeoning efforts for new, even-more-brilliant fourth generation sources, it seems clear that XPCS studies of the dynamics of condensed matter ought to be on every Research Director's list of future scientific directions.

However, because XPCS has proven so challenging, it is currently only possible to carry out XPCS experiments that go beyond demonstrations at a few beamlines around the globe. These include ESRF beamline 10-ID, where efforts have focussed on measurements at short time scales – in some cases less than a microsecond – using a single-channel, hardware correlator. In this way, it has been possible, for example, to study the dynamics of suspensions of metallic particles[6], the dynamics of freely-suspended smectic liquid crystal membranes, by monitoring the scattering at wavevectors near the smectic-A phase Bragg peak[7], or the capillary dynamics of liquid surfaces[8]. Because of the use of a single detector channel, experiments at 10-ID usually have involved very strong scatterers. This has often limited the length scales that have been studied to those usually accessible to optical techniques. However, the samples studied at 8-ID typically cannot be studied optically, because they are opaque, or the order-parameter is modulated, *etc*.

XPCS experiments using soft x-rays have been carried out at the ALS by Sorensen, Kevan and coworkers, who also studied the dynamics of freely-suspended smectic liquid crystal membranes by monitoring the scattering at wavevectors near the smectic-A phase Bragg peak, also using a single-channel correlator[9].

At 8-ID at the Advanced Photon Source, we have pursued a complementary approach, based on an area detector. It was realized several years ago[10,11] that by using a CCD-based area detector, consisting of 10^6 pixels, to acquire data from many coherence areas (speckles) simultaneously, it might be possible to lessen the difficulties posed by the low x-ray count rates at large wavevectors. Our strategy at 8-ID has been to employ not only beamline optics suitable for XPCS, but we have also emphasized samples that exhibit slower dynamics, and the implementation of CCD detectors for XPCS, together with the requisite data acquisition and analysis tools[12,13]. Currently, at 8-ID, it is possible to study dynamics on time scales of several milliseconds or longer, at wavevectors that exceed what can be reached in light scattering by a factor of 5 or more, depending on the sample scattering strength.

III Coherent x-ray beams

Key to performing XPCS measurements is a coherent or partially coherent x-ray beam. What is a coherent beam? Crudely, we can say that for a sample illuminated by a partially coherent beam the value of the electric field at a given point in the sample has a more-or-less definite phase relationship to the field at another, distant point in the sample. If such a beam is used in a scattering experiment, fluctuations in the scattered intensity arise as a result of interference among the wave fields scattered by different parts of the sample. This is speckle. Furthermore, for samples undergoing thermal fluctuations, the time autocorrelation function of the speckle pattern yields the characteristic times of the sample. This is the PCS technique.

The coherence of a photon beam has two components: transverse or lateral coherence and longitudinal or temporal coherence. For a synchrotron source of x-rays, with an approximately Gaussian intensity distribution, far from the source, the transverse "one-sigma" coherence lengths at the sample are $\xi = \lambda R/(2\pi\sigma_x)$ in the horizontal direction and $\zeta = \lambda R/(2\pi\sigma_z)$ in the vertical direction, where λ is the x-ray wavelength, σ_x and σ_z are the "one-sigma" source sizes in the horizontal and vertical directions, respectively, and R is the source-to-sample distance.

It is possible to create a partially-transversely coherent beam by aperturing any x-ray beam to have transverse dimensions that are on the order of the transverse coherence lengths. Only at high-brilliance third generation sources, however, do a sufficient number of photons for XPCS pass through such an aperature. The role of brilliance can be seen as follows: The number of photons per second per unit solid angle from a source of brilliance B is the product of the source area and the brilliance, or approximately $\pi B\sigma_x\sigma_z$. The transversely coherent flux is the number of photons

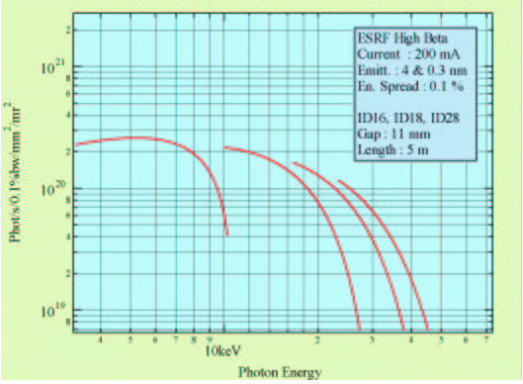

FIG. 1: Brilliance of several undulators at the ESRF.

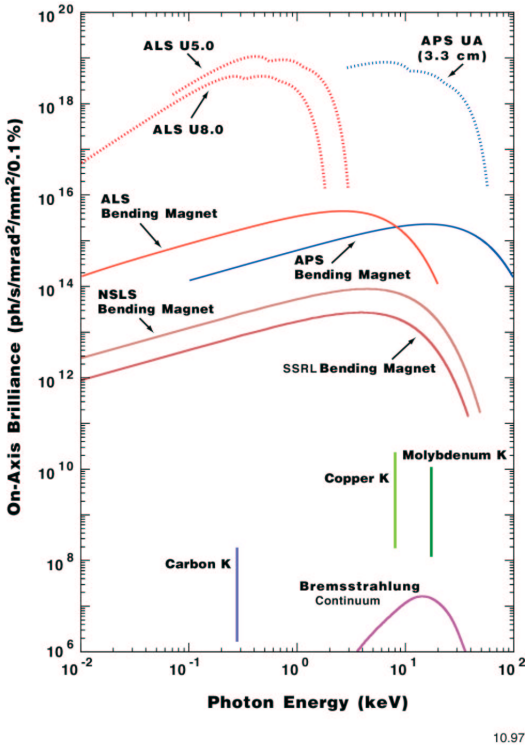

FIG. 2: Brilliance of Undulator A at the APS in comparison with several other sources.

that pass through the solid angle corresponding to the coherence lengths, *i.e.* $\pi\xi\zeta/R^2$. Thus, the transversely coherent flux is approximately

$$\pi^2 B\sigma_x\sigma_y\xi\zeta/R^2 = B\lambda^2/4. \quad (2)$$

Evidently, the more brilliant the source, the greater the transversely coherent flux. In July 2003, the highest brilliance that I could find quoted was for several beamlines at the ESRF. As shown in Fig. 1, these are in the 10^{20} range for 6 keV-xrays. In comparison, Fig. 2 shows an older plot of the brilliance versus energy for several sources, including APS UA, which is what is in place at 8-ID. This gives a brilliance in the 10^{19} range at 6 keV. All of the experiments that I will describe were carried out using APS undulator A.

In addition to the transverse coherence, we also need partial longitudinal coherence for XPCS. The longitudinal coherence length of the beam is given by $\Lambda \simeq \lambda(E/\Delta E)$, where E is the photon energy, and ΔE is the full-width-at-half-maximum (FWHM) of the energy spectrum. Partial longitudinal coherence requires that the optical path length difference (δ) between x-rays scattered from different parts of the sample should not be more than a few times Λ. For a transmission geometry, there are two contributions to δ. The first, which arises because of a non-zero width (L) of the illuminated portion of the sample within the scattering plane, is $\delta_L = 2L(Q/k)\sqrt{1-Q^2/k^2}$. The second comes from the non-zero sample thickness and is $\delta_W = 2WQ^2/k^2$. All of the measurements that I will describe were carried out in the small angle regime, so that $Q \ll k$. It follows, in the case of monochromatic beam ($\Delta E/E \simeq 10^{-4}$), that $\delta \ll \Lambda$. In addition to monochromatic beam, for an undulator source with a spectrum consisting of successive harmonics, it is possible to create so-called "pink-beam" by causing the raw undulator beam to be reflected from a flat mirror. This essentially eliminates x-rays with energies greater than the critical energy for total external reflection. The pink-beam spectrum approximates a single peak with $\Delta E/E \simeq 0.026$ FWHM, so that $\Lambda \geq \delta$.

As shown in Ref. 12, in the often-realistic limit that the illuminated sample dimensions exceed their respective coherence lengths, the degree of coherence is given more-or-less by the ratio of the coherence volume to the illuminated sample volume, *i.e.*

$$\beta = \frac{\pi\Xi Z\Lambda}{LM\delta} \quad (3)$$

for pink beam, and

$$\beta = \frac{\pi\Xi Z}{LM}, \quad (4)$$

for monochromatic beam, where Ξ and Z are the *effective* horizontal and vertical coherence lengths, respectively, taking into account the detector resolution in addition to the source size.

IV Beamline 8-ID

A Layout

8-ID now consists of an optics enclosure and two experimental hutches. The first key feature of 8-ID is a 0.3 mm diameter water-cooled aperture, that passes only the central cone of undulator radiation. The next beamline component is a silicon mirror; only x-rays with energies lower that the critical energy (12 keV) for total external reflection are passed by the mirror. These two optics ensure that only the minimum necessary heat load is passed downstream, while the beam

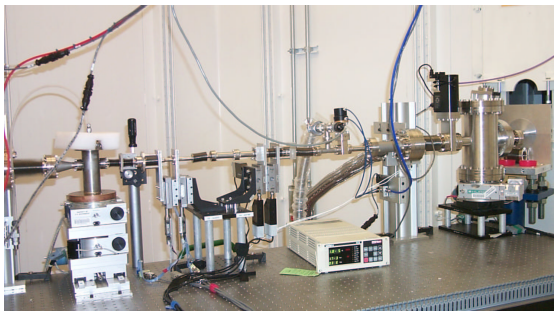

FIG. 3: Picture of the 8-ID XPCS setup. Key components from right to left are: monochromator, beam-cross-section-defining slits, guard slits, sample chamber. The CCD is not shown and is located 3 m further to the left.

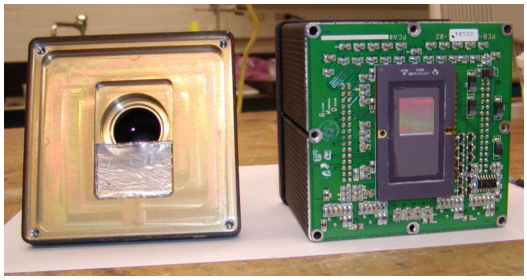

FIG. 4: Photograph of our new, fast x-ray detector for XPCS. The x-ray window is removed revealing the CCD chip itself.

brilliance is maintained. Next, for the side-station (8-ID-E), comes a single bounce sideways-deflecting silicon monochromator, set for Bragg reflection at an energy of 6.7 keV, which intercepts one-half of the x-ray beam, leaving the undeflected portion to propagate to the end station (8-ID-I), where there is a double-bounce germanium monochromator. Thus, when the undulator is set to place the first harmonic at 6.7 keV, two experiments can be run simultaneously, each using an undulator beam of uncompromised brilliance. Initially, we chose to run at 7.65 keV, but more recently we have picked 6.7 keV as an improved compromise between maximizing the efficiency of our CCD detectors and minimizing attenuation in beamline beryllium windows, etc.

Located in 8-ID-I is our small-angle XPCS spectrometer, which is shown in Fig. 3. This instrument permits measurements over a range in wavevectors from 0.01 nm^{-1} or less, to about 0.5 nm^{-1}. Before the sample, in-vacuum slits define a partially-coherent beam and guard against scatter. Since the coherent flux is directly proportional to the beam brilliance, it essential that the beamline optics preserve as far as possible the brilliance. To this end, there are currently only two polished Be windows between the undulator and the sample. After the sample, the scattered speckle pattern is collected using a CCD-based detector system. Our XPCS methodology involves acquiring time-resolved sequences of x-ray scattering patterns (speckle patterns) and then determining the time intensity autocorrelations from these sequences.

B CCD-based x-ray detectors

Recently, we have made notable progress in two aspects related to the detector. One improvement is the development of new, faster and much more user-friendly XPCS data reduction software, principally by graduate student Matt Borthwick. This is now installed at 8-ID-I as a standard part of our XPCS package. An even more important improvement in our XPCS capability follows from our recent implementation – principally by graduate student Peter Falus – of a new, fast, CCD-based x-ray detector for time-resolved x-ray scattering experiments. The key feature of this camera – the SMD1M60 — as a detector for XPCS experiments is that it permits us to continuously acquire images, consisting of individual photon events, at full-frame data rates of up to 60 Hz and one-sixteenth-frame data rates of up to 500 Hz. Thus, it is straightforward to acquire data with a time resolution of as little as 2 ms, and data from a considerably larger solid angle can be collected if a time resolution of 17 ms is acceptable. In comparison to our earlier generation detectors, the much greater data rate possible with the SMD1M60 permits a many-fold increase in the XPCS SNR in cases where sub-second time steps are called for. In addition, the SMD1M60 is based on an inexpensive, comercially-available CCD camera. It is also lightweight and conveniently transportable. Beyond XPCS, we expect that this detector may find application in time-resolved x-ray scattering experiments of all sorts. We have also found it capable of collecting superior small angle x-ray scattering (SAXS) data. A picture of the camera with its x-ray window removed to reveal the CCD chip is shown in Fig. 4.

To highlight where it is valuable to use a CCD and where it is best to use a single-channel hardware correlator, we may introduce the expression, derived by Jakeman[14], for the SNR in an XPCS experiment. In its simplest form, valid at low count rates, and adapted for CCDs, Jakeman's expression reads

$$SNR_{CCD} = \beta i \sqrt{T\tau_a}\, \eta \sqrt{\tau_a F}\, \sqrt{n_x n_y} \qquad (5)$$

where η is the quantum efficiency, *i.e.*, the probability of detecting an x-ray photon with the camera, $n_x n_y$ is the number of pixels per frame, β is the optical contrast, i is the count rate per pixel, T is the total measurement time, F is the frame rate, and τ_a is the accumulation time. In general, the frame rate is related to the minimum delay time between successive images (τ_d) via $1/F = \tau_d$. For an ideally-ef£cient ($\eta = 1$), single

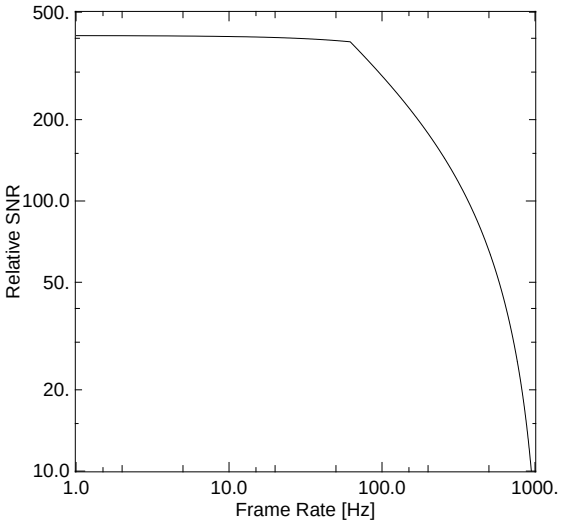

FIG. 5: XPCS SNR for the SMD1M60 CCD-based detector relative to an ideally ef£cient, ideally-fast, single-channel, hardware correlator.

channel ($n_x n_y = 1$) fast detector, we have that

$$SNR_1 = \beta i \sqrt{T/F}. \tag{6}$$

To compare the relative merits of single-channel and CCD-based detectors, we may simply calculate the relative SNR, *i.e.* ratio of Eq. 5 to Eq. 6,

$$\frac{SNR_{CCD}}{SNR_1} = \eta \tau_a F \sqrt{n_x n_y}. \tag{7}$$

For the SMD1M60, operating at frame rates less than $F_{max} = 62$ Hz, $\eta \simeq 40\%$, $n_x n_y = 1024 \times 1024$, and $\tau_a = 1/F - \tau_t$, where $\tau_t = 840\ \mu$s is the frame transfer time. For higher frame rates, the number of pixels that can be read out is reduced according to

$$n_x n_y = 1024 \times 1024 \times \frac{F_{max}(1 - \tau_t F)}{F(1 - \tau_t F_{max})} \tag{8}$$

The relative SNR is plotted versus frame rate in Fig. 5. Clearly, the CCD-based detector has a superior SNR to a point detector for frame rates up to F_{max} and somewhat beyond. However, if it is desired to examine processes that relax on sub-millisecond time scales, the CCD-readout time becomes a limitation. Clearly, even faster detectors would bene£t XPCS greatly.

V Pink-beam aerogel speckle

Aerogel is a fixed assembly of small silica droplets, arranged in a random, fractal network. Ordinarily, the small angle x-ray scattering (SAXS) from an aerogel would appear as in Fig. 7 (taken from Ref. 1), which shows the measured x-ray scattering cross-section of 3.4 mm-thick, 0.0287 g cm^{-3} (86%void) silica aerogel, averaged over rings at fixed Q, plotted versus Q.

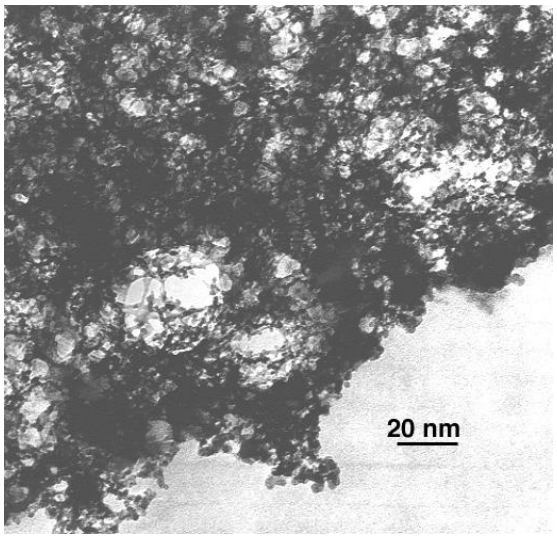

FIG. 6: Transmission electron micrograph of silica aerogel from `http://eande.lbl.gov/ECS/aerogels/saphoto.htm`.

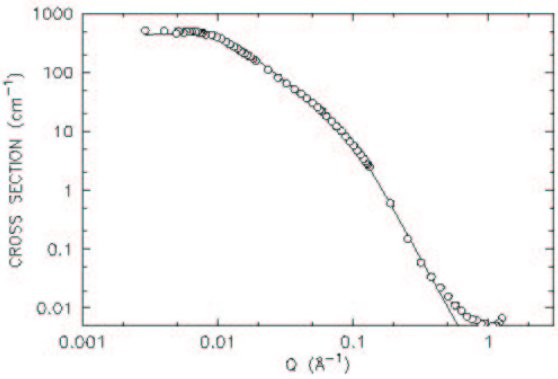

FIG. 7: Measured (open circles) and model (line) x-ray scattering cross-sections of 3.4 mm-thick, 0.0287 g cm^{-3}-dense silica aerogel, averaged over rings at fixed Q, versus Q.

The open circles are data; the solid line is a simple model. At the largest Qs, the upturn in the data corresponds to an intermolecular distance within the silica and is not included in the model. For Qs between about 0.1 and 0.5 Å^{-1}, both the data and the model follow Porod's law, *i.e.* the cross-section varies as Q^{-4}. This is scattering from the silica-vacuum interfaces. Between about 0.01 and 0.1 Å^{-1}, corresponding to length scales from 60 to 600 Å, the data and the model vary as $Q^{-2.1}$ corresponding to a fractal structure within this range of length scales with a fractal dimension of $d_f = 2.1$. Finally, for Qs less than about 0.01 Å^{-1}, the cross-section no longer corresponds to a fractal. Instead, it can be understood in terms of the hard-sphere-like packing of more-or-less spherical objects – presumably silica clusters with an internal fractal structure – so that the weak peak at about 0.01 Å^{-1} corresponds to the cluster-cluster separation. In fact,

the actual scattering from which Fig. 7 was derived looked quite similar to Fig. 8 (taken from Ref. 15), which shows the scattering from a 1.6 mm-thick, 95%-void aerogel sample, obtained using the pink beam at 8-ID. with slits before the sample, set to be 4 μm in the horizontal direction and 11 μm in the vertical direction. The detector used was a CCD 2.34 m downstream of the sample. This sample is static. Therefore, the time-averaged intensity is strongly modulated in a random fashion by virtue of the partially coherent illumination. This is x-ray speckle. Averaging over many speckles, as for Fig. 7, nevertheless leads to the usual SAXS profile.

Fig. 9, taken from Ref. 15, shows the probability density of the speckle intensity $[p(I)]$ within a ring at 0.086 nm^{-1} of width 0.0014 nm^{-1}. Perfectly coherent illumination, corresponding to a single mode, gives rise to an exponential $p(I)$. Partially-coherent illumination produces speckle that may be considered to be the sum of m modes, and we can expect $p(I)$ to be the convolution of m exponentials, *i.e.*

$$p(I) = m^m (I/\bar{I})^{m-1} e^{-mI/\bar{I}} / (\Gamma(m)\bar{I}), \qquad (9)$$

where $\Gamma(m)$ is the gamma function, and $< I >$ is the mean intensity. The distribution described by Eq. 9 is shown as the line in Fig. 9. In an XPCS measurement, the zero-time intercept of the intensity-intensity correlation function, *i.e.* β, is related to m via $\beta = 1/m$. Thus, we refer to β as the "speckle contrast"

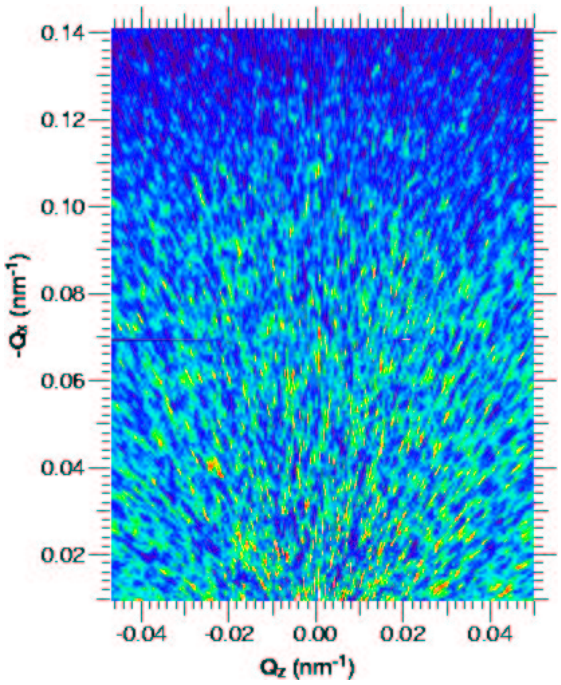

FIG. 8: Speckle pattern obtained from a 0.5 mm-thick aerogel sample plotted on a false color scale versus scattering vector. Blue regions indicate less scattering, red regions more scattering.

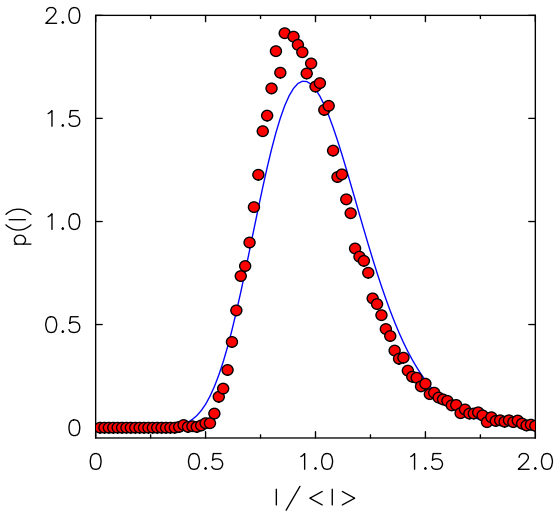

FIG. 9: Measured speckle intensity distribution (circles) compared to the model (line) described in the text.

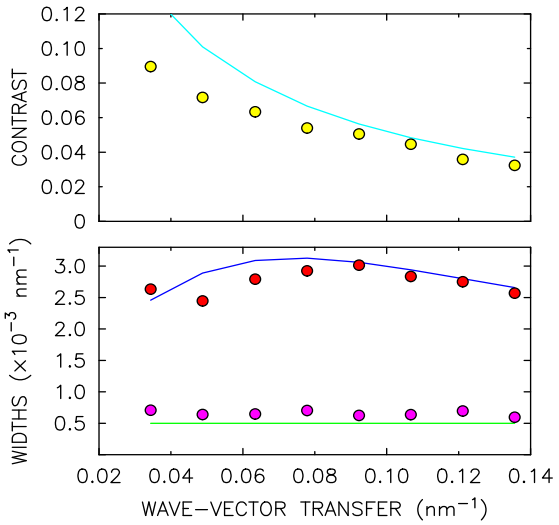

FIG. 10: Top: Measured speckle constrast (circles) vs. wavevector compared to theory (line). Bottom: Measured speckle widths (circles) in the radial (larger width) and transverse (smaller width) directions vs. wavevector, compared to theory (lines).

or "contrast". The top panel of Fig. 10, also from Ref. 15 shows the variation of the speckle contrast with wavevector in comparison to what may be expected for the experimental configuration used[16]. The decrease in contrast with increasing wavevector is a result of the fairly broad bandpass of the pink beam. The lower panel shows the corresponding experimental (circles) and theoretical (lines) speckle widths in the radial (larger width) and transverse (smaller width) directions, determined from the spatial autocorrelation function of the speckle pattern Clearly, it is possible to create partially-coherent x-ray beams with more-or-less the expected coherence.

VI Collective diffusion in concentrated colloidal suspensions

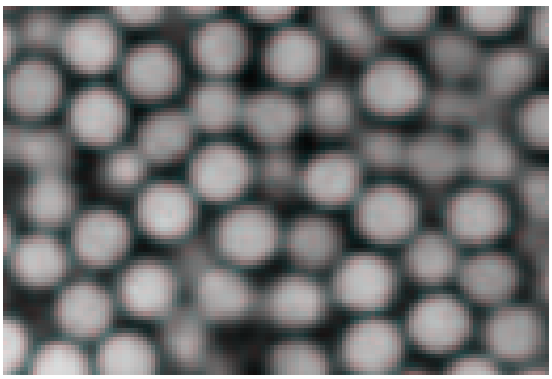

FIG. 11: Confocal microscope image of a colloidal glass from Eric Weeks' web site at Emory University.

In the process of developing a new method – *e.g.* XPCS – it is important to demonstrate early on that the results obtained are meaningful. We therefore decided to look first for a model system to study, for which there were both available theoretical predictions and prior experimental results that we could make contact with, as well as scientific reasons for a new study. Thus, the first XPCS experiments that we initiated at 8-ID were SAXS and XPCS experiments to study the structure and dynamics of suspensions of polystyrene (PS) latex spheres of radius $R = 66.5$ nm, suspended in glycerol for various sphere volume fractions (ϕ)[2,3]. Spherical particles of this size yield characteristic, readiliy-observable SAXS patterns. In addition, the dynamics of dilute suspensions of spherical particles are well understood. In particular, it is well-known that colloidal diffusion in dilute suspensions is governed by the diffusion equation:

$$\frac{\partial \rho}{\partial t} = D_0 \nabla^2 \rho, \qquad (10)$$

where ρ is the deviation from a uniform density, $D_0 = k_B T/6\pi\eta R$ is the Stokes-Einstein diffusion coefficient. (k_B is Boltzmann's constant, T is the absolute temperature, η is the viscosity of the suspending medium, and R the sphere radius.) However, for concentrated suspensions, the dynamics are still not fully understood after more than 25 years of research[17–23], and remain an active area[24–26].

The significance of our measurements in connection with XPCS was that they demonstrated that this technique may yield reliable data of sufficiently high quality to go beyond demonstrations and examine in-depth the dynamics of opaque soft matter. In particular, we were able to show good agreement between XPCS measurements and detailed calculations of the short-time diffusion coefficient of a hard sphere suspension for a range of concentrations from dilute to the crystallization limit, showing that the results of XPCS measurements are credible. Other groups have also employed XPCS for detailed studies of concentrated colloidal suspensions[27]. For these and the other XPCS measurements described in this lecture, we used monochromatic beam in order, first, to be able to have a constrast of 0.1-0.2 with 50×50 μm^2 slits, and, second, to avoid the rapid sample beam damage and heating that can occur with pink beam.

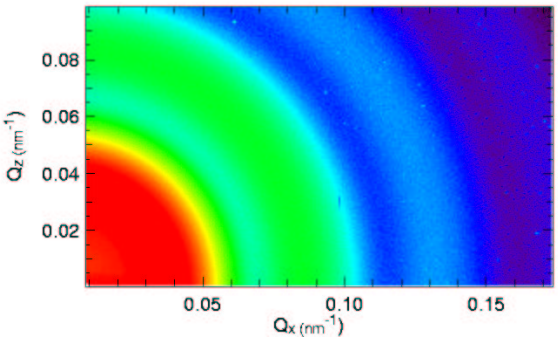

FIG. 12: False color image of the SAXS from a sample of PS latex in glycerol at a volume fraction of $\phi = 0.28$, obtained using a direct illumination CCD from Princeton Instruments. The isolated bright spots are pixel defects.

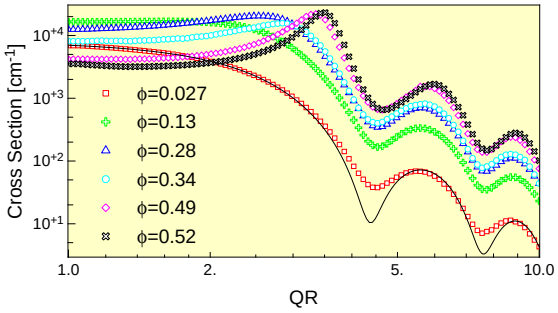

FIG. 13: Cross-section for several different volume fractions of PS spheres in glycerol vs. *QR*.

A SAXS from colloidal hard spheres

Representative SAXS from a PS-in-glycerol sample with $\phi = 0.28$ is shown in Fig. 12. This image represents the time average of the scattering over approximately 10 minutes. In comparison to Fig. 8, the intensity in Fig. 12 varies smoothly from pixel to pixel. This is because the latex-in-glycerol sample is dynamic, so that its microscopic configuration varies on a time scale short compared to 10 minutes, washing out the speckle contrast.

By circularly averaging the sort of data shown in Fig. 12, we obtain the x-ray scattering cross-section. This is displayed in Fig. 13 for samples of differing volume fractions and for wavevectors from $QR = 1$ to $QR = 10$. At large QR, the shape of the scattering ap-

pears independent of volume fraction and shows intensity oscillations characteristic of uniform spheres. Actually, the solid line in Fig. 13 shows the best fit to the $\phi = 0.027$-data of a model for the scattering of hard spheres with a volume fraction of 0.027 and a relative polydispersity in radius of 0.025, as per the manufacturer's specification. The sole fitting parameter was the mean particle radius, resulting in a best-fit value of 66.5 nm. We ascribe the discrepancies that appear at the scattering minima for $QR > 3$ to small departures of the latex particles from spherical symmetry.

At smaller wavevectors, a pronounced peak develops as the volume fraction increases, corresponding to increasing interparticle correlations. This behavior is highlighted in Fig. 14, which shows the structure factor, obtained by dividing the measured scattering for different volume fractions by the particle form-factor, determined from the $\phi = 0.027$-data, after applying a small structure factor correction. The data of Fig. 14 are analogous to the liquid structure factor of an atomic fluid. The principle peak of the structure factor approaches $QR \simeq 3.5$ at large volume fractions, consistent with what may be expected for hard spheres. The solid lines in Fig. 14 correspond to the Percus-Yevick structure factor for hard spheres[28] with a mean radius of 66.5 nm. The model was fit to the measured structure factor, varying only the volume fraction for each data set.

Evidently, the hard-sphere model provides a good description of the experimental structure factors at all volume fractions, in particular reproducing the position of the principle peak accurately. In addition, the behavior of the measured structure factor at small wavevectors is reproduced well by the model. This informs us that the osmotic compressibility of PS in glycerol is well described by the hard sphere equation of state. Gratifyingly, the best-fit values for the volume fractions of the different samples are indistinguishable from the nominal volume fractions.

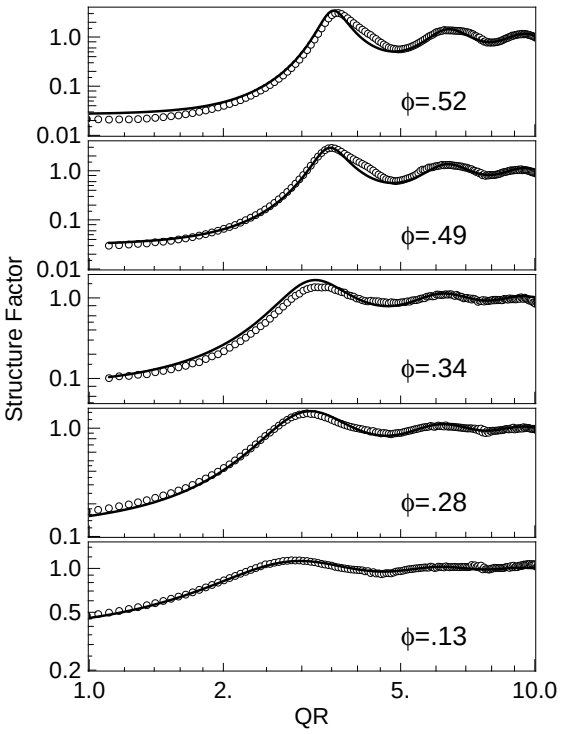

FIG. 14: Interparticle structure factor for PS latex spheres in glycerol for volume fractions of 0.027 (squares), 0.13 (pluses), 0.28 (triangles), 0.34 (circles), 0.49 (diamonds), and 0.52 (crosses), shown on a log-log scale. The solid line is the expected structure factor for particles with a mean radius of 66.5 nm.

B The intermediate scattering function for diffusion

Before turning to our XPCS measurements, we consider what we should expect for $S(Q,t)$. How to calculate $S(Q,t)$ is described in detail in, for example, Ref. 5 or in Ref. 29. In brief, however, the prescription is as follows. First, we determine the steady-state response of the system of interest to a harmonically-varying field, that is conjugate to the the order parameter. For the density (ρ), the congujate field is the chemical potential (μ), and Eq. 10 leads to

$$-i\omega\tilde{\rho}(Q,\omega) = -DQ^2[\tilde{\rho}(Q,\omega) - \chi(Q)\tilde{\mu}(Q,\omega)], \tag{11}$$

where the tilde indicates a spatial and temporal Fourier transform, ω and Q are the corresponding angular frequency and wavevector, respectively, and $\chi(Q)$ gives the density response to a static Q-dependent chemical potential. Eq. 11 implies that the so-called dynamic suceptibility [$\chi(Q,\omega)$] for diffusion is given by

$$\chi(Q,\omega) = \frac{\tilde{\rho}(Q,\omega)}{\tilde{\mu}(Q,\omega)} = \frac{\chi(Q)DQ^2}{-i\omega + DQ^2}. \tag{12}$$

Next, we invoke the fluctuation-dissipation theorem. Ordinarily, when it is evaluated at imaginary frequencies, the dynamic suspectibility exhibits simple poles. In this case, the fluctuation-dissipation theorem informs us that $S(Q,t)$ is given by a sum of modes, labelled by index p:

$$S(Q,t) = \Sigma_p^{\infty} C_p \exp(-\Gamma_p t), \tag{13}$$

where the mode decay rates [$\Gamma_p = \Gamma_p(Q)$] correspond to the poles in question, *i.e.*

$$\chi^{-1}(Q, \omega = -i\Gamma_p) = 0, \tag{14}$$

while the mode amplitudes [$C_p = C_p(Q)$] are related to the corresponding residues, via

$$C_p = \frac{k_B T}{\Gamma_p} Residue\ \chi(Q, -i\Gamma_p). \tag{15}$$

For Eq. 12, there is only one pole with the result that

$$S(Q,t) = k_B T \chi(Q) \exp(-DQ^2 t). \tag{16}$$

C XPCS from colloidal hard spheres

Representative intensity autocorrelation functions (g_2) for time delay from 30 ms to 300 s, obtained at $QR = 1.5$, 3.5, and 6.0, for $\phi = 0.28$ and $\phi = 0.52$ are shown in Fig. 15 and Fig. 16, respectively. For $\phi = 0.28$, single exponential fits [lines in Fig. 15] provide a good description of the autocorrelations, consistent with expectations based on Eq. 16. For $\phi = 0.52$, however, the observed g_2 are not single exponentials. However, in the limit of both the short and long times, they vary exponentially, as shown by the red and blue line segments in Fig. 16. Thus, we may identify corresponding short-time and long-time diffusion coefficients, D_S and D_L, respectively. Specifically, D_S (D_L) is related to the short-time (long-time) time decay time, τ_S (τ_L), via $\tau_S = 1/(D_S Q^2)$ [$\tau_L = 1/(D_L Q^2)$].

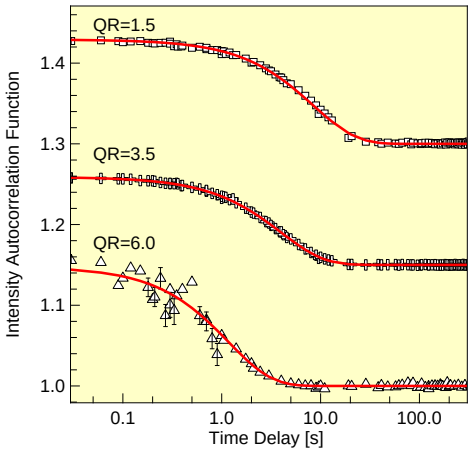

FIG. 15: Autocorrelations, $g_2(Q,t)$, for $\phi = 0.28$ for $QR = 1.5$ (offset by 0.3), $QR = 3.5$ (offset by 0.15), and $QR = 6.0$.

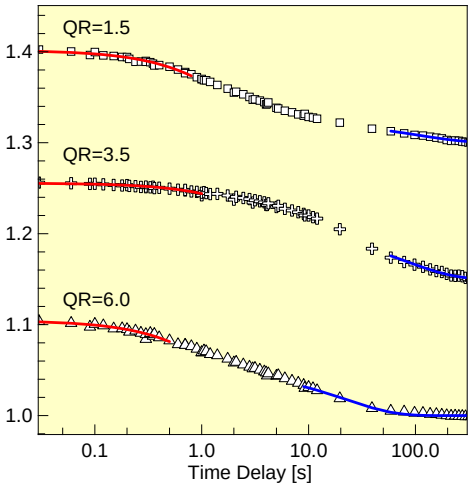

FIG. 16: Autocorrelations, $g_2(Q,t)$, for (b) $\phi = 0.52$ for $QR = 1.5$ (offset by 0.3), $QR = 3.5$ (offset by 0.15), and $QR = 6.0$.

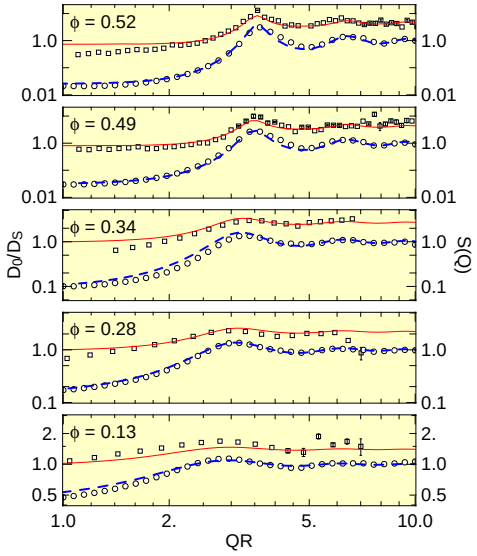

FIG. 17: Measured and theoretical D_0/D_S (squares and solid lines, respectively) and $S(Q)$ (circles and dashed lines, respectively) vs. QR for PS spheres in glycerol.

D "de Gennes-narrowing"

The open squares in Fig. 17 show D_0/D_S versus Q for each sample. The most striking feature of these results is that D_0/D_S displays a peak that mimics the peak in the static structure factor[19,20,22–24,26], reproduced as the open circles in Fig. 17 together with the model hard-sphere structure factor (blue dashed line). Since a peak in D_0/D_S corresponds to a peak in τ_S, this informs us that configurations of low free energy, signalled by a peak in the structure factor, are also long-lived, which seems to make physical sense. In fact, this phenomenon occurs very generally and is known as "de Gennes narrowing"[30].

Analytic calculations of the Q-dependence of D_0/D_S for hard spheres, carried out by Beenakker and Mazur[21], are illustrated as the red solid lines in Fig. 17. There is good agreement at all volume fractions with no adjustable parameters. On this basis, it seems reasonable to proceed assuming that XPCS is indeed a viable method for investigating the dynamics of soft matter and indeed can yield credible, high-quality data on systems of interest.

E Foreshadowing the glass transition

The non-single-exponential behavior at larger volume fractions foreshadows a transition to a glassy phase at even higher volume fractions[31]. Actually, in a different colloidal, hard-sphere system, Segre and Pusey[25] discovered that (for a given ϕ) $\ln f(Q,t)/[D_S(Q)Q^2]$ is a function solely of time between $QR = 2.5$ and 6. Fig. 18 shows our results for

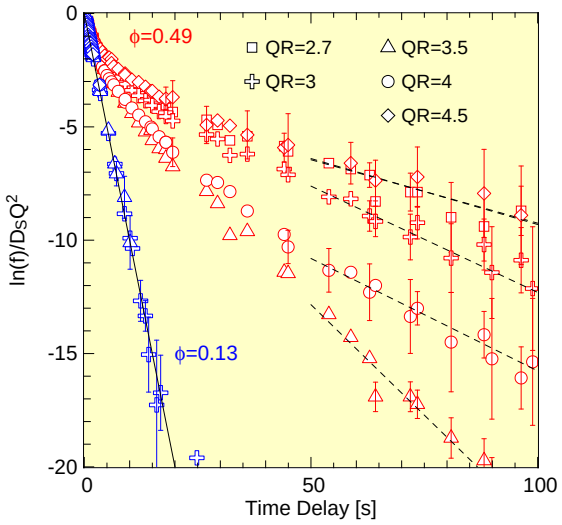

FIG. 18: Scaled ISF at several wavevectors for $\phi = 0.13$, and $\phi = 0.49$.

this quantity for $\phi = 0.13$ and 0.49. The $\phi = 0.13$-data scales to a straight line with a slope of -1, corresponding to a single exponential decay. By contrast, at $\phi = 0.49$, the data deviate from a straight line, corresponding to a non-single-exponential decay. More significantly, unlike in Ref. 25, these data do not collapse to a single scaling form. This discrepancy is not understood and illustrates there are still things to learn about the dynamics of hard sphere colloids.

VII Surface dynamics of polymer films

FIG. 19: Sunset in Alaska.

Although the surface modes of viscoelastic liquids were predicted[32,33] to be strongly overdamped with relaxation times determined by the viscosity (η), surface tension (γ), film thickness (h), and wavenumber (Q), there had been no experimental tests of how these theories might apply to thin films, and in particular to polymer thin films. This is especially interesting in the context of recent experiments that indicate that the glass transition temperature near polymer surfaces is lower than in the bulk[34–40]. One method that may in principle be employed to characterize the dynamics of polymer films is to measure the spectrum of thermal surface capillary waves using scattering methods[41]. Such an experiment directly measures the relaxation of thermal fluctuations in the surface height. Because the wavevectors achieved in SAXS are well matched to the height of typical surface asperities and the thicknesses of typical thin films, we were motivated to employ XPCS as a method for studying surface and thin film dynamics using a reflection geometry, in which the x-ray beam impinges on the sample at grazing incidence and the g_2 are measured on the diffusely scattered (off-specular) x-rays[8].

We have characterized the surface dynamics of supported polystyrene (PS) films as a function of lateral length scale, film thickness, and temperature. The results of this study were first reported in Ref. 42.

A Near-specular surface scattering

Fig. 20(a) illustrates the scattering geometry. By arranging for the x-ray incidence angle (0.14°) to lie below the critical angle for total external reflection (0.16°), we were able to restrict the x-ray penetration into the film to a depth of ~ 90 Å, far less than any of the film thicknesses studied here. Thus, scattering from the film-substrate interface is negligible, and only fluctuations of the polymer/vacuum interface are probed. Specifically, within the distorted-wave Born approximation (DWBA)[43], we have

$$\frac{d\sigma}{d\Omega} \simeq |T(\alpha_i)|^2 |T(\alpha_e)|^2 \frac{k_B T}{\gamma q_{||}^2}, \qquad (17)$$

where k_B is Boltzmann's constant, T is the absolute temperature, γ is the surface tension, and $q_{||}$ is the wavevector transfer in the plane of the surface. $T(\alpha_i)$ and $T(\alpha_e)$ are the Fresnel transmission coefficients for the incidence angle (α_i) and exit angle (α_e), respectively. Fig. 20(b) shows a false-color CCD image of the time-averaged diffuse scattering from the 840 Å-thick film at 160°C. In comparison, Fig. 20(c) represents the static structure factor calculated on the basis of the capillary wave model[44–46]. The good agreement between the experimental data and the model confirms that the surface morphology is governed by capillary waves. Furthermore, the surface tension so-obtained is in good agreement with literature values[47].

The intensity oscillations apparent in the figure, which occur as a function of the exit angle with respect to the surface, originate in an interference between x-rays that are scattered directly into the detecter, and those that are first scattered towards the substrate, and subsequently reflected back from the substrate into the detector. Mathematically, the origin of this behavior

lies in the oscillatory variation of the Fresnel transmission coefficient (which determines the electric field just at the surface of the film) versus exit angle for the case of a film on a substrate, which appears in the DWBA expression for the scattering from surface roughness[43] (Eq. 17). This is illustrated in the upper panel of Fig. 21, which plots the absolute square of $T(\alpha)$ versus angle (α). The angle α can be either the incidence or exit angle. In the lower panel of this figure, we show the electric field intensity for 7.65 keV x-rays within a 80 nm-thick PS film on a flat Si substrate, averaged over the thickness of the film, plotted versus incidence angle[48]. Interestingly, at the specific angles at which $|T(\alpha)|^2$ shows dips, the mean intensity in the interior of the film can greatly exceed the incident field. This may be valuable in facilitating future experiments that focus on the dynamics of fluctuations within the film, rather than of its surface.

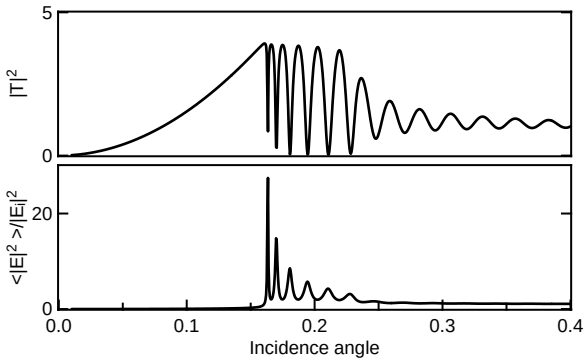

FIG. 21: Upper panel: Fresnel intensity transmission coefficient for 7.65 keV x-rays incident on a 80 nm-thick polystyrene film (critical angle 1.6°) supported on a flat Si substrate (critical angle 0.23°), plotted *vs.* incidence angle. Lower panel: Electric field intensity for 7.65 keV x-rays within a 80 nm-thick PS film on a flat Si substrate, averaged over the thickness of the film, plotted *vs.* incidence angle.

B Surface XPCS

Representative experimental g_2s, acquired from a 840 Å-thick film at 160°C, are shown as the solid symbols in Fig. 22 for four different in-plane wavevectors [$q_{||}$]. The solid lines in Fig. 22 represent the best single-exponential fits to the measured autocorrelations at each value of the wavevector parallel to the surface (in-plane wavevector, $q_{||}$) *i.e.* $g_2 = 1 + \beta \exp(-2t/\tau)$, where β is the speckle contrast and $\tau = \tau(q_{||})$ is the relaxation time for equilibrium surface height fluctuations. The parameters varied in each fit were β and τ. Evidently, the model provides a good description of our data.

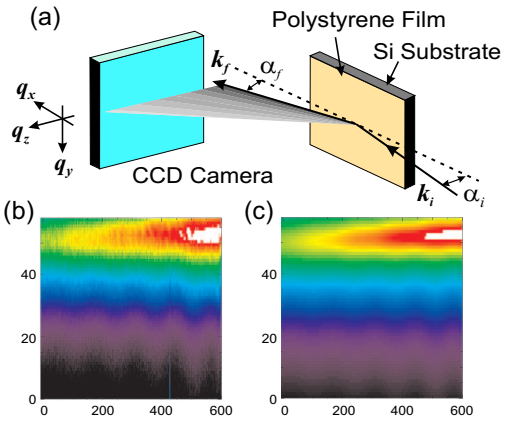

FIG. 20: (a) The schematic reflectivity geometry in XPCS. (b) The CCD image of time-averaged diffuse scattering and (c) the fit to capillary wave model with a sample having thickness of 840 Å at 160°C. The numbers in x- and y-axis in (b) and (c) are corresponding pixels. The range of exit angles corresponding to the data in (b) and (c) is from 0.3° to 0.55°.

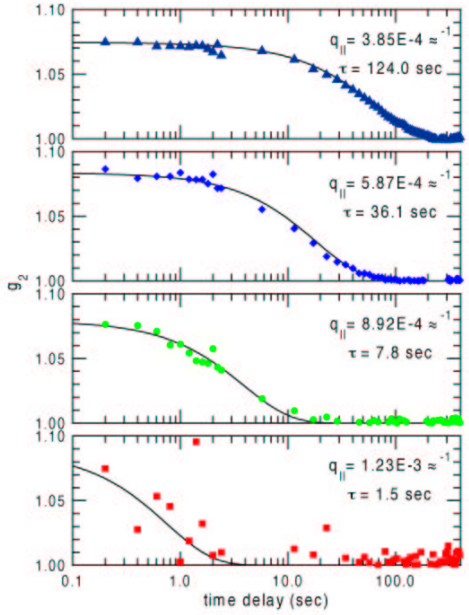

FIG. 22: Autocorrelations obtained at four different in-plane wavevectors measured in a sample thickness of 840 Å at 160°C (solid symbols) in comparison with the results of single exponential fits (solid lines). The time constant τ at each $q_{||}$ is also displayed.

The $q_{||}$-dependence of the best-fit relaxation times is displayed in Fig. 23(a) at three different temperatures for the 1770 Å-thick film. The time constants for 170°C are fastest, those for 160°C are slower, and those for 150°C are slowest. In each case, however, the $q_{||}$-dependence appears to be similar, with larger length-scale asperities relaxing more slowly than

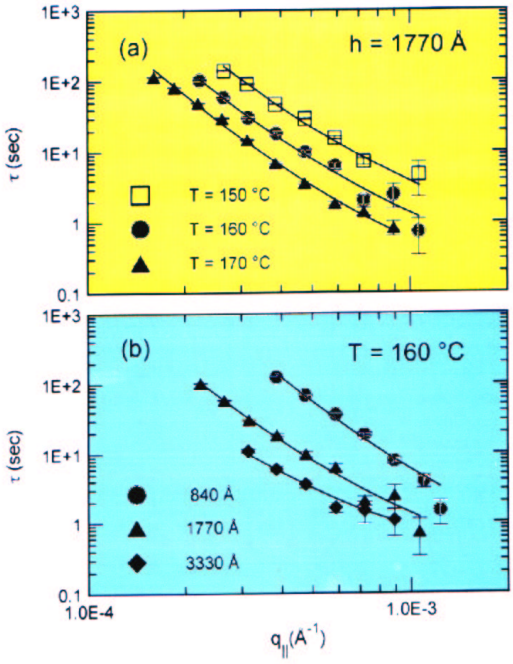

FIG. 23: (a) Measured time constant (τ) *vs.* in-plane wavevector ($q_{||}$) for the 1770 Å-thick film at 150 °C (squares), 160 °C (circles), and 170°C (triangles). Lines correspond to the model described in the text. (b) τ *vs.* $q_{||}$ at 160 °C for films of thickness 840 Å(circles), 1770 Å(triangles), and 3330 Å(diamonds). Lines correspond to the model described in the text.

smaller ones. Shown in in Fig.23(b) are the relaxation times at 160°C for the three different-thickness films. In this case, the time constants are largest for the thinnest film and decrease monotonically with increasing thickness. The fact that the surface dynamics depend on film thickness demonstrates that, although our measurements are sensitive only to surface motions, those motions in turn depend on molecular movements throughout the film.

C The intermediate scattering function for overdamped capillary relaxations

An explicit prediction for the intermediate scattering function for the surface height fluctuations of uniform, thin films follows from the theory of the dynamic susceptibility given in Ref. 33, using just the prescription given above. Specifically, for parameter values appropriate to the surface of liquid polystyrene, $S(Q,t)$ should decay essentially single-exponentially in time with a relaxation time, $\tau(q_{||})$, given by

$$\tau(q_{||}) \simeq \frac{2\eta[\cosh^2(q_{||}h) + {q_{||}}^2h^2]}{\gamma q_{||}[\sinh(q_{||}h)\cosh(q_{||}h) - q_{||}h]}. \qquad (18)$$

Eq. 18 indicates that τ/h should be directly proportional to the ratio η/γ and otherwise solely a function of $q_{||}h$. To test the predicted scaling behavior, we have plotted the quantity $\tau(q_{||})/h$ versus $(q_{||}h)$ for all films studied at 150°C, 160°C, and 170°C in the main panel of Fig. 24. At each temperature, data from the three different samples collapse to form a single curve, confirming the anticipated scaling with film thickness. The solid lines in Fig. 24 correspond to the best fits of the data to Eq. (18). Since the film thicknesses are known, it is notable that excellent agreement between theory and experiment is achieved with a single fitting parameter, namely the ratio η/γ. These results are strong evidence that Jäckle's theory is satisfactory, and that its premise of a wavevector- and thickness-independent viscosity is appropriate for the films studied here.

We may go further and inquire as to the value of the thin film viscosity and, in particular, how it compares to the viscosity of bulk PS. As noted above, static diffuse scattering measurements[49] determine the surface tension (γ) to be independent of film thickness and, to be consistent with the surface tension of bulk PS (~ 30 mN/m) [47]. Knowing the surface tension (γ), we may obtain the film viscosity (η), because the fits to $\tau(q_{||})/h$ versus $q_{||}h$ determine η/γ. Thus, the film viscosity is plotted versus temperature in the inset of Fig. 18, together with the corresponding bulk viscosity[50]. Evidently, bulk and film viscosities are identical within errors.

In light of the reports of a near surface T_g suppression, it is interesting to ask whether our measurements tell us that there is no surface layer of substantially different viscosity? After all, if T_g near the surface is suppressed, there might also be a suppression of the near-surface viscosity even above T_g. Would such a low-viscosity near-surface layer affect the capillary mode frequencies? To answer this question, one can perform a calculation of $S(q_{||},t)$ for an *inhomogeneous* film composed of two layers of differing viscosity. Taking the densities of the layers to be equal and for there to be no interfacial tension between them, the final result for the slowest relaxation mode of this two-layer liquid film is

$$\Gamma = -q_{||}\gamma\Big(2hq_{||}(\eta_1+\eta_2)+2q_{||}z(\eta_1-\eta_2)\cosh(2q_{||}(h-z))+2q_{||}(\eta_1-\eta_1)(h-z)\cosh(2q_{||}z)-(\eta_1+\eta_2)\sinh(2hq_{||})$$
$$-(1+2{q_{||}}^2z^2)(\eta_1-\eta_2)\sinh(2q_{||}(h-z))-(\eta_1-\eta_2)\sinh(2q_{||}z)\Big)$$
$$\times\Big(2(1-2{q_{||}}^2z^2){\eta_1}^2+2(1+2{q_{||}}^2(h^2+2z^2))\eta_1\eta_2+4{q_{||}}^2(h^2-z^2){\eta_2}^2+2\eta_1(\eta_1+\eta_2)\cosh(2hq_{||})$$
$$+2(\eta_1-\eta_2)$$
$$\times[(1+2{q_{||}}^2z^2)\eta_1\cosh(2q_{||}(h-z))+(\eta_1+2{q_{||}}^2(h-z)^2\eta_2)\cosh(2q_{||}z)$$
$$-2q_{||}z\eta_1\sinh(2q_{||}(h-z))-2q_{||}(h-z)\eta_2\sinh(2q_{||}z)]\Big)^{-1}, \qquad (19)$$

where h is the total film thickness, and z is the thickness of the surface layer with viscosity η_2. η_1 is the vicosity of the layer adjacent to the substrate, which, of course, has thickness $h-z$. (If I was ever in doubt about the value of Mathematica, this formulae put rest to it.)

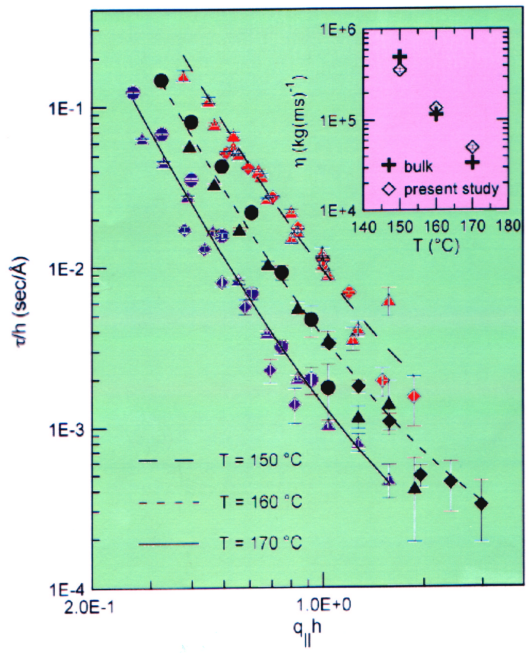

FIG. 24: τ/h *vs.* $q_{||}h$ for all three films of thickness 840 Å(circles), 1700-1770 Å(triangles), and 3180-3330 Å(diamonds). Lines at 150°C (long dashed line), 160°C (dashed line), and 170°C (solid line) correspond to Eq. (18). Inset: Viscosity of thin-film PS (diamonds) and bulk PS (crosses) *vs.* temperature.

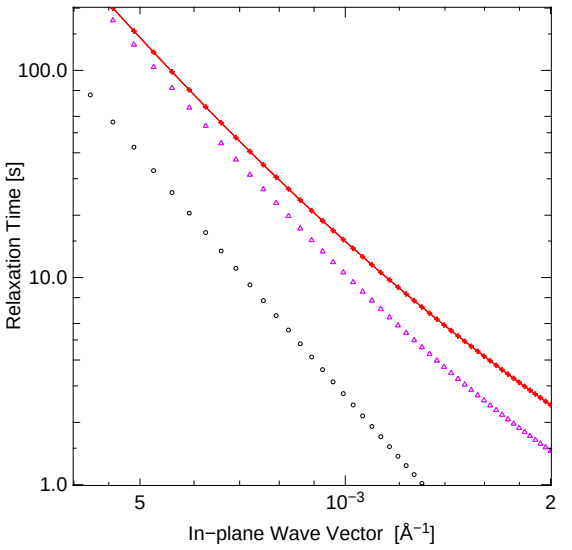

FIG. 25: Variation of τ *vs.* $q_{||}$ for an $h = 80$ nm-thick homogeneous film with a visosity of $\eta_1 = 3.5\times10^5$ kg m^{-1} s^{-1} = η_2 (solid red line and red crosses), for an inhomogeneous film of total thickness equal to $h = 80$ nm of which the surface-most $z = 10$ nm has a viscosity of $\eta_2 = 3.5\times10^4$ kg m^{-1} s^{-1} while the remaining 60 nm has a viscosity of $\eta_1 = 3.5\times10^5$ kg m^{-1} s^{-1} (magenta triangles), and for an inhomogeneous film of total thickness equal to $d = 80$ nm of which the surface-most $z = 10$ nm has a viscosity of $\eta_2 = 3.5\times10^2$ kg m^{-1} s^{-1} while the remaining 60 nm has a viscosity of $\eta_1 = 3.5\times10^5$ kg m^{-1} s^{-1} (black squares). It may seem that one thousand fold different viscosities is extreme. However, near T_g, the viscosity varies very rapidly versus temperature.

If, following Kawana and Jones, we take the surface layer thickness to be 10 nm, then on the basis of a detailed analysis of Eq. 19 in comparison to our data, then – as illustrated in Fig. 25 – we may conclude that, at least down to 150°C, there is no evidence for a 10-nm thick surface layer with a viscosity that differs from the bulk viscosity by more than a factor of ten. It is important to state that this conclusion does not necessarily contradict the notion of a near-surface T_g suppression – it may be that different processes with different temperature dependences determine the near-surface viscosity in different temperature regimes, and that a cross-over to a different regime may occur closer to T_g than studied here. Nevertheless, our measurements and analysis provide an important constraint on theories seeking to explain the viscosity near a poly-

mer surface and any posible near-surface reduction in T_g.

Clearly, in order to come to a more definite conclusion concerning the question of a near surface suppression of T_g at polymer surfaces, it will be important to extend our initial measurements (i) to shorter length scales (larger $q_{||}$s), (ii) to lower temperatures that lie closer to T_g, (iii) to a wider range of film thicknesses, especially thinner films (iv) to different molecular weights, and (v) to different substrate terminations. However, beyond the surface dynamics of PS thin films, these initial results demonstrate that SXPCS is an exciting new research opportunity and they provide encouragement for further work to study the dynamics of all sorts of surface fluctuations and fluctuations within thin films Fig. 21).

VIII Polymeric sponge phase dynamics

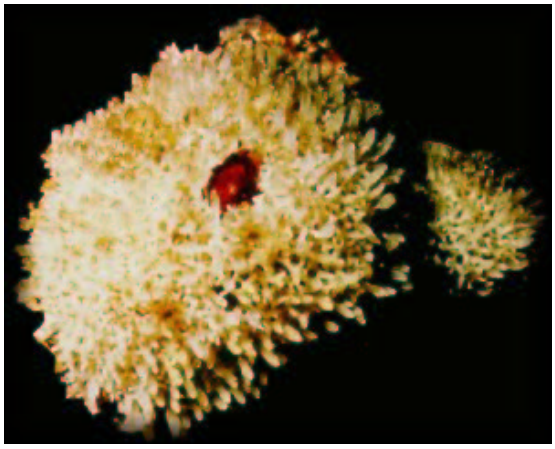

FIG. 26: *Leucosolenia eleanor* from `http://www.mareco.org`.

Complex fluids comprise a large and diverse collection of molecular systems. An especially important class of complex fluids, however, involves amphiphilic molecules, *i.e.* molecules with end groups that interact unfavorably. In order to keep these unfavorably interacting groups separated, amphiphilic materials tend to self-assemble into more-or-less complicated morphologies with characteristic length scales that can vary from from nanometers to micrometers.

In order to understand the basic principles of self-assembly and thus be able to rationally control and design amphiphilic behavior, a great deal of attention has been focussed on model systems, often composed of water and/or an alkane and a small molecule surfactant. In several respects, however, polymeric complex fluids, containing block copolymers perhaps blended with homopolymer, are preferable model systems.

The simplest block copolymer is an AB diblock, consisting of a sequence, or block, of (say) A monomers chemically bound to a block of B monomers. A symmetric ABA triblock would be an A block, followed by a B block, followed in turn by an A block, identical to the first. Such materials are amphiphilic because the energy cost of placing an A monomer next to a B monomer, exceeds that of placing A next to A and B next to B. For basic studies, a key advantage of polymer-based systems in comparison to those involving small-molecules is that the former's macromolecular character leads to universal behavior, dependent on only a few parameters. Specifically, melt and blend polymers can accurately be described as Gaussian chains, with segment length a_A and polymerization index N_A (for A chains), and the molecular interactions between A and B segments can be described via a Flory-Huggins parameter χ. So-called self-consistent field theory (SCFT) permits essentially exact calculations of the structure and phase behavior of ordered block copolymer systems, which agree remarkably well with experiment. Even for disordered phases SCFT should be able to provide accurate free energies for the constituents of the phase in question, which can then be used as input to statistical mechanical calculations. Therefore, in contrast to the situation that holds for small-molecule complex fluids, where the best that can be achieved is to interprete experiments in terms of phenomenological parameters, experiments with polymer amphiphiles offer the prospect of an essentially microscopic, first-principles understanding of complex fluid phase behavior, structure, and dynamics.

Experiments on copolymer melts and copolymer-homopolymer blends reveal a remarkable variety of ordered structures, including lamellar (L_α), hexagonal (H), *a.k.a* cylindrical (C), body-centered cubic (BCC), *a.k.a.* spherical (S), double-diamond (D), perforated lamellar (PL) and gyroid (G) phases, some of which are schematically illustrated in Fig. 27. However, some of the most intriguing and generic phases found in small-molecule complex fluids are disordered, and have not yet been fully characterized in polymer systems. These include so-called sponge phases, which occur in amphilphilic solutions containing an amphilphile and water (or oil), where the amphiphiles self-assemble into extended, random, multiply-connected bilayer membranes[52–54], arranged so that the hydrophobic (or hydrophilic) moieties are protected on the interior of the bilayer. Fig. 28, taken from Ref. 55, shows the results of a Monte Carlo simulation of a sponge phase. Sponge phases are quintessential complex fluids. Their microstructures are themselves fascinating. In addition, sponge phases can in principle exhibit a variety of interesting phase transitions.

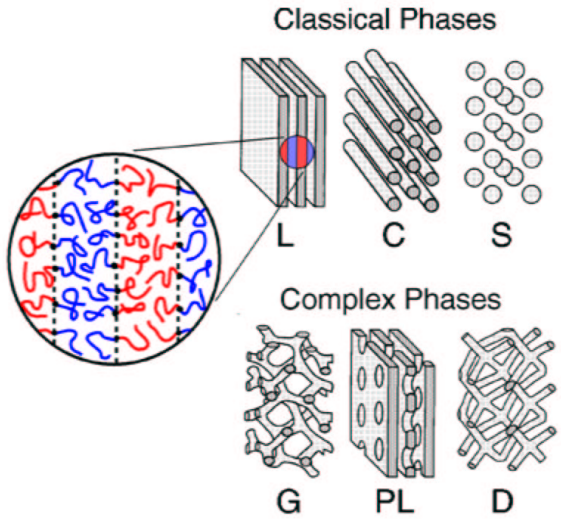

FIG. 27: Block copolymer morphologies from Ref. 51. The expanded view of the L_α phase shows individual polymers.

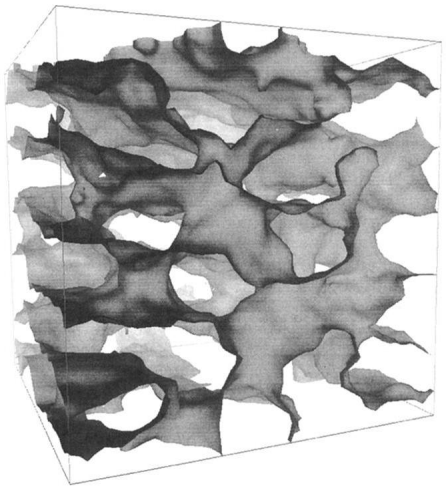

FIG. 28: Putative sponge phase morphology from Monte Carlo simulations.

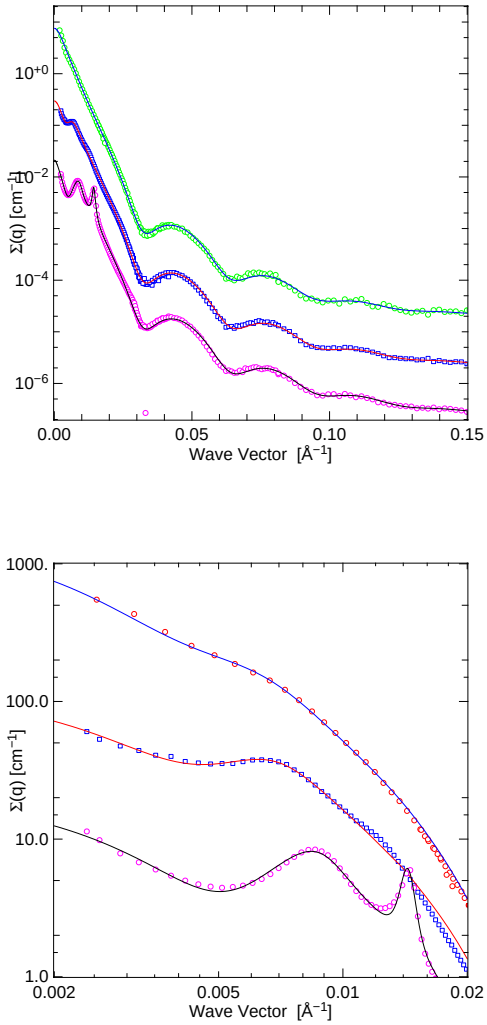

FIG. 29: Top: Scattering from PS-P(SEBS) blends for wavevectors from 0.0 to 0.15 $Å^{-1}$. Bottom: Scattering from PS-P(SEBS) blends for wavevectors from 0.002 to 0.02 $Å^{-1}$.

A SAXS from a polymeric sponge

To create a sponge phase in a polymer system, to permit a first-principles understanding of its structure and dynamics, and its phase transitions, entropy must be introduced. One way to increase the entropy compared to a strictly long-chain system is to blend a relatively short-chain homopolymer with a long-chain block copolymer. We chose to use a symmetric ABA triblock copolymer blended with A homopolymer. That this receipe indeed yields a polymeric sponge, is shown in Fig. 29, which shows the small angle x-ray scattering (SAXS) from blends of $M_w = 87$k poly(styrene-ethylene/butylene-styrene) (PSEBS) triblock copolymer with $M_w = 3.5$k polystrene (PS) at 160°C. The top panel plots these data on a logarithmic intensity scale and a linear wavevector scale from 0.00 to 0.15 $Å^{-1}$. The lower panel uses a log-log scale and focusses on the low-wavevector scattering between 0.002 and 0.02 $Å^{-1}$. In both panels, the same data are shown, corresponding to samples with PSEBS volume fractions of 0.19, 0.30, and 0.40, from top to bottom. For clarity, the 0.40-volume-fraction data have been mutiplied by 0.01 and the 0.30-volume-fraction data by 0.1.

The top panel of Fig. 29 reveals that an important feature of the data at larger wavevectors is the presence of prominent intensity oscillations with a period of 0.032 $Å^{-1}$, which appear in all of the profiles. The locations of the oscillation minima are inconsistent with scattering from either spheres or cylinders, which would also produce oscillatory scattering intensities. Instead, these data unambigiously point to

a nanoscale structure that consists predominantly of poly(ethylene/butylene) (PEB) sheets, or *membranes*, of thickness $d = 190$ Å.

Focussing now on the 0.30-volume fraction sample, CCD images (not shown) show that the structure factor is isotropic. In addition, as is evident from the lower panel of Fig. 29, there is a relatively large peak at zero scattering vector, and a smaller peak at a wavevector of 0.007 Å^{-1}. To what phase does this scattering correspond? The isotropy of the SAXS pattern tends to rule out the L_α phase, and in fact, the existence of an isotropic scattering profile with a larger peak at zero wavevector and a smaller peak at non-zero wavevector is generally taken as a signature of the L_3 phase. Accordingly, given also that its structure is built out of membranes, we identify 0.30-volume-fraction P(SEBS) in PS as an L_3 phase. For the 0.19-volume fraction data there is a peak at zero wavevector, but instead of a distinct peak at non-zero-wavevector there is a shoulder. Nevertheless, these data too are consistent with an L_3 phase.

By the time the volume fraction is increased to 0.40, the L_3-phase peak has moved to $Q_3 = 0.0085$ Å^{-1} and the correlation length (ξ), given roughly by the inverse of the peak width, has increased noticably. In addition, a third peak has appeared at a wavevector of about $Q_\alpha = 0.014$ Å^{-1}. For these data, examination of the CCD images reveals that, while the putative L_3 phase peak remains isotropic, the peak at 0.014 Å^{-1} shows azimuthal variations, indicating that this peak corresponds to the textured powder peak of a liquid crystal phase, and that at a volume fraction of 0.40 there is coexistence between the L_3 phase and this liquid crystal phase. Because we observe a solitary liquid crystal peak, and because the ratio $Q_\alpha/Q_3 \simeq 1.5$ is what is found at L_3-L_α coexistence in small-molecule systems, we identify this liquid crystal as a lamellar L_α phase.

The solid lines in Fig. 29 show the results of preliminary fits of the data to the model form given by Gompper and Schick[56] for the L_3 phase scattering, modified to account for a finite, instead of infinitesimal, membrane thickness. (For the 0.40-volume fraction data, we have also added a peak for the L_α phase.) Evidently, the model provides an excellent description of the experimental SAXS profiles over the entire range of volume fractions, wavevectors and intensities studied, further confirming that PSEBS in PS constitutes an L_3 phase at least for volume fractions from 0.19 to a little less than 0.40.

B Sponge phase dynamics

Beyond the static structure and phase behavior, a major part of our motivation for pursuing a polymeric L_3 phase is, of course, to be able to carry out XPCS experiments on a system with thermal fluctuations that relax on accessible time scales. However, the sponge phase scattering is considerably weaker than for the previous two examples. Fortunately, the new SMD1M60 detector had become available and was used for the £rst time to carry out XPCS measurements on the sponge phase. Fig. 30 shows representative intensity-intensity correlation functions, obtained with the SMD1M60, plotted versus time on a logarithmic scale, obtained for a L_3 phase sample at 140°C.

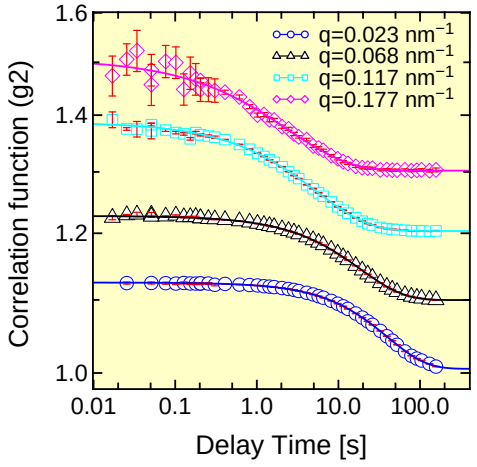

FIG. 30: Intensity-intensity autocorrelation functions (g_2) *vs.* delay time for an L_3-phase sample of P(SEBS) triblock copolymer in short-chain PS homopolymer at 140°C at wavevectors of 0.023, 0.068 and 0.117 and 0.177 nm^{-1}. For clarity, the $g2$s are displaced by 0.3, 0.2, 0.1, and 0.0, respectively.

It is notable that while these data extend from a shortest delay time of 17 milliseconds to 200 seconds – *i.e.* more than a factor of 10^4 in time – the signal-to-noise ratio even at the shortest times is excellent at the smallest and intermediate wavevectors, and in all cases is sufficient to accurately establish the value of g_2 in the short-time limit. The quality of these data is much superior to what would have been possible with our previous generation of detector. Indeed, in addition to obtaining values for the characteristic relaxation time and its wavevector dependence, it will now be routinely feasible to investigate the lineshape of g_2, possibly permitting detailed comparisons with theory. The solid lines shown in Fig. 30 are fits to a stretched exponential form:

$$g_2 = 1 + \beta \exp[2(t/\tau)^\alpha], \qquad (20)$$

with characteristic relation time τ and stretching exponent α. This form was chosen in an ad-hoc fashion in order to be able to provide a good account of the measured g_2s and thus permit a straightforward, preliminary determination of the characteristic relaxation time (τ). Nevertheless, the fits describe the experimental data very well, and certainly are better than would have been obtained using a single exponential form. The relaxation times so-determined at 140 °C are shown

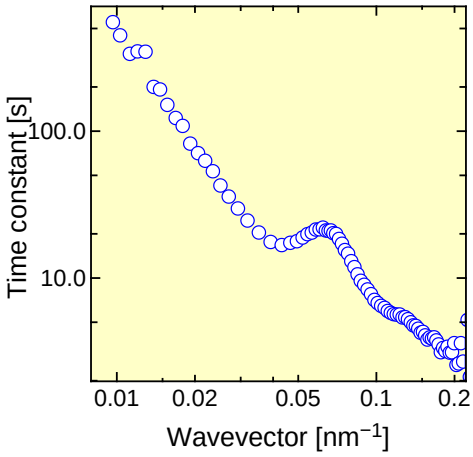

FIG. 31: Relaxation time *vs.* wavevector for a 20% P(SEBS)-80% PS blend at 140°C, plotted on logarithmic axes.

in Fig. 31. At the smallest wavevectors investigated ($q < 2k$), the time constant varies approximately as the inverse square of the wavevector, consistent with relaxation via a diffusion-like process. Near wavevectors corresponding to the peak of the static structure factor, however, the relaxation time deviates from a simple power law and itself shows a peak versus wavevector. This is *de Gennes narrowing* again in a different context. For wavevectors between $2k$ and 0.02 Å^{-1}, the relaxation time varies approximately as the inverse first power of the wavevector. For wavevectors beyond 0.02 Å^{-1}, where the scattering intensity is decreasing rapidly with increasing wavevector, the SNR becomes too poor for a determination of the relaxation time.

The dynamics that may be expected in the sponge phase have attracted considerable theoretical interest. At small wavevectors, there is general agreement that the dynamics should be diffusive, *i.e.* that $\tau = 1/(Dq^2)$. Specifically, for example, Milner *et al.* have proposed that $D \simeq k_B T/\eta\xi$, where ξ is the correlation length, given by the inverse of the peak width, and η is the solvent – the PS homopolymer – viscosity. The PS homopolymer viscosity is a well-known function of temperature, and the correlation length can be determined via SAXS. Therefore, we are planning further XPCS and SAXS measurements for different volume fractions and at different temperatures in order to investigate how well this prediction matches with experiment.

For wavevectors near $2k$, where the static structure factor shows a peak, Hennes and Gompper[57], for example, also predict a peak. This is qualitatively consistent with our data (Fig. 31), and with the general notion of *de Gennes narrowing*. Again, XPCS and SAXS measurements at different volume fractions will further elucidate this behavior.

Interestingly, it is for wavevectors within the range $2k < q < 2\pi/d$, that the theoretical predictions seem most clear, and yet most at variance with what we observe. Specifically, Zilman and Granek[58] treat the sponge phase scattering in the range $2k < q < 2\pi/d$ as originating from a collection of isolated membrane "plaquettes". This leads to the prediction that in this regime

$$\tau \simeq (\kappa/k_B T)^{1/2}(\eta/k_B T q^3), \qquad (21)$$

where κ is the membrane bending modulus. Evidently, the prediction is that the relaxation time varies as the inverse third power of the wavevector. Experimentally, we observe a variation as the inverse £rst power. The origin of this discrepancy is unclear. However, a signi£cant difference between our polymeric surfactant system and small molecule surfactant systems, where the wavevector scaling predicted by Zilman and Granek is observed[59,60], is that in our system the membrane thickness is a large fraction of the membrane separation, in contrast to theory which assume thin membranes. In addition, because of entanglements, polymeric systems can be viscoelastic. In the case of a polymer membrane, we may anticipate a response that re¤ects a non-zero elastic modulus (G) at non-zero frequencies. In turn, this may lead to qualitatively different relaxation than for the strictly ¤uid membranes envisaged by Zilman and Granek[58].

IX Conclusion and Prospects

XPCS is a promising, new method for examining the slow dynamics of condensed matter on shorter length scales than can be achieved via light scattering techniques. Currently, the accessible time scales are well-matched to polymeric systems. However, we can crudely estimate the enhancement in the SNR that can be be expected from fairly straightforward improvements relative to the current setup at 8-ID. These include vertical focussing ($\times 5$), use of a wider band-pass monochromator, such as an asymmetrically-cut crystal pair ($\times 2$), better preservation of beam coherence through improved windows and re¤ecting optics ($\times 3$). Thus, we may hope to "easily" realize a gain in the SNR of XPCS experiments of about 30. Such a gain would greatly extend the range of physical problems that could be addressed.

Unfortunately, this gain does not come without a potential cost. The cost is that the x-ray ¤ux on the sample is correspondingly increased, with an increased possibility for x-ray damage. This does not present a problem in some cases, but for soft-matter systems, it seems certain that the implementation of strategies to ameliorate the effect of x-ray sample damage will be necessary and I would like to encourage the study of this issue. Of course, the damage issue is not peculiar to XPCS but is important for any susceptible system studied at the third generation. One approach suitable for some, but not all, experiments would be to implement a ¤ow cell for XPCS experiments with a narrow

channel. Here, the ¤ow must be suf£ciently slow that the decay of intensity correlations is due to the relaxation of microscopic ¤uctuations within the sample, rather than due to the macroscopic ¤ow. It must also be suf£ciently fast that the time-integrated x-ray damage does not affect the sample's microscopic dynamics.

Finally, let me note that looking further ahead, XPCS is one of the motivations for the fourth generation.

References

[1] A. R. Sandy, L. B. Lurio, S. G. J. Mochrie, A. Malik, G. B. Stephenson, and M. Sutton. Production and characterization of x-ray speckle at Sector 8 of the Advanced Photon Source. *SPIE proceedings*, 3154:27, 1997.

[2] L. B. Lurio, D. Lumma, P. Falus, M. A. Borthwick, S. G. J. Mochrie, J.-F. Pelletier, M. Sutton, A. Malik, and G. B. Stephenson. Absence of scaling for the intermediate scattering function of a hard-sphere suspension: static and dynamic x-ray scattering from concentrated polystyrene latex spheres. *Phys. Rev. Lett.*, 84:785, 2000.

[3] D. Lumma, L. B. Lurio, A. R. Sandy, M. Borthwick, P. Falus, S. G. J. Mochrie, M. Sutton, and L. Regan. Structure and dynamics of concentrated dispersions of polystyrene latex spheres in glycerol: Static and dynamic x-ray scattering. *Phys. Rev. E*, 62:8258, 2000.

[4] H. J. Kim, A. Ruehm, L. B. Lurio, J. Basu, J. Lal, S. G. J. Mochrie, and S. K. Sinha. X-ray photon correlation spectroscopy on polymer £lms with molecular weight dependence. *Physica*, 336:211–215, 2003.

[5] D. Forster. *Hydrodynamic Fluctuations, Broken Symmetry, and Correlation Functions*. Benjamin, Reading, MA, 1975.

[6] T. Thurn-Albrecht, W. Steffen, A. Patkowski, G. Meier, E. W. Fisher, G. Grübel, and D. L. Abernathy. Photon correlation spectroscopy of colloidal palladium using a coherent x-ray beam. *Phys. Rev. Lett.*, 77:5437–5440, 1996.

[7] I. Sikharulidze, I. P. Dolbnya, A. Fera, A. Madsen, B. I. Ostrovskii, and W. H. de Jeu. Smectic membranes in motion: Approaching the fast limits of x-ray photon correlation spectroscopy. *Phys. Rev. Lett.*, 88:115503, 2002.

[8] T. Seydel, A. Madsen, M. Tolan, G. Grubel, and W. Press. Capillary waves in slow motion. *Phys. Rev. B*, 63:3409, 2001.

[9] A. C. Price, L. B. Sorensen, S. D. Kevan, J. Toner, A. Poniewierski, and R. Holyst. Coherent soft-x-ray dynamic light scattering from smectic-A £lms. *Phys. Rev. Lett.*, 82:755, 1999.

[10] A. P. Y. Wong and P. Wilzius. Dynamic light scattering with a CCD camera. *Rev. Sci. Instrum.*, 64:2547, 1993.

[11] S. B. Dierker, R. Pindak, R. M. Fleming, I. K. Robinson, and L. E. Berman. X-ray photon correlation spectroscopy study of Brownian motion of gold colloids in glycerol. *Phys. Rev. Lett.*, 75:449–452, 1995.

[12] D. Lumma, L. B. Lurio, S. G. J. Mochrie, and M. Sutton. Area detector-based photon correlation in the regime of short data batches: data reduction for dynamic x-ray scattering. *Rev. Sci. Instrum.*, 71:3274, 2000.

[13] P. Falus, M. Borthwick, and S. G. J. Mochrie. A fast ccd-based area detector for x-ray photon correlation spectroscopy and time-resolved x-ray scattering. *Rev. Sci. Instrum.*, In preparation, 2003.

[14] E. Jakeman. Photon correlation. In H. Z. Cummins and E. R. Pike, editors, *Photon Correlation and Light Beating Spectroscopy*, pages 75–149. Plenum, New York, 1973.

[15] L.B. Lurio, D. Lumma, M. A. Borthwick, P. Falus, S. G. J. Mochrie, J. F. Pelletier, and M. Sutton. Creating coherent x-rays and putting them to use: X-ray photon correlation spectroscopy at beamline 8-id at the advanced photon source. *Synchrotron Radiation News*, 13:28, 2000.

[16] A. R. Sandy, L. B. Lurio, S. G. J. Mochrie, A. Malik, G. B. Stephenson, J.-F. Pelletier, and M. Sutton. Design and characterization of an undulator beamline optimized for small-angle coherent x-ray scattering at the Advanced Photon Source. *J. Synchrotron Rad.*, 6:1174, 1999.

[17] B. J. Ackerson. Correlations for interacting Brownian particles. *J. Chem. Phys.*, 64:242, 1976.

[18] A. R. Altenberger. On the wave vector dependent mutual diffusion of interacting Brownian particles. *J. Chem. Phys.*, 70:1994, 1979.

[19] J. C. Brown, P. N. Pusey, J. W. Goodwin, and R. H. Ottewill. Light scattering study of dynamic and time-averaged correlations in dispersions of charged particles. *J. Phys. A*, 8:664, 1975.

[20] F. Grüner and W. Lehmann. The *k* dependence of the long-time diffusion in systems of interacting Brownian particles. *J. Phys. A: Math. Gen.*, 12:L303–L307, 1979.

[21] C. W. J. Beenakker and P. Mazur. Diffusion of spheres in a concentrated suspension II. *Physica A*, 126:349, 1984.

[22] W. van Megan, R. H. Ottewill, S. M. Owens, and P. N. Pusey. Measurement of the wave-vector dependent diffusion-coef£cient in concentrated particle dispersions. *J. Chem. Phys.*, 82:508–515, 1985.

[23] A. P. Philipse and A. Vrij. Determination of static and dynamic interactions between monodisperse, charged silica spheres in an optically matching, organic solvent. *J. Chem. Phys.*, 88:6459, 1988.

[24] P. N. Segre, O. P. Behrend, and P. N. Pusey. Short-time Brownian motion in colloidal suspensions – experiment and simulation. *Phys. Rev. E*, 52:5070, 1995.

[25] P. N. Segre and P. N. Pusey. Scaling of the dynamic scattering function of concentrated colloidal suspensions. *Phys. Rev. Lett.*, 77:771, 1996.

[26] J. K. Phalakornkul, A. P. Gast, R. Pecora, G. Nägele, A. Ferrante, B. Mandl-Steininger, and R. Klein. Structure and short time dynamics of polydisperse charge-stabilized suspensions. *Phys. Rev. E*, 54:661, 1996.

[27] D. O. Riese, G. H. Wegdam, W. L. Vos, R. Sprik, D. Feinstein, J. H. H. Bongaerts, and G. Grübel. Effective screening of hydrodynamic interactions in charged colloidal suspensions. *Phys. Rev. Lett.*, 85:5460, 2000.

[28] W. L. Grif£th, R. Triolo, and A. L. Compere. Analytical structure function of a polydisperse Percus-Yervick ¤uid with Schultz (gamma) distributed diameters. *Phys. Rev. A*, 33:2197, 1986.

[29] P. M. Chaikin and T. C. Lubensky. *Principles of Condensed Matter Physics*. CUP, Cambridge, UK, 1995.

[30] P. G. de Gennes. Liquid dynamics and inelastic scattering of neutrons. *Physica*, 25:825–839, 1956.

[31] W. van Megan and P. N. Pusey. Dynamic light scattering study of the glass transition in a colloidal suspension. *Phys. Rev. A*, 43:5429, 1991.

[32] J. L. Harden, H. Pleiner, and P. A. Pincus. *J. Chem. Phys.*, 94:5208, 1991.

[33] J. Jackle. The spectrum of surface waves on viscoelastic liquids of arbitrary depth. *J. Phys. Condens. Matter*, 10:7121, 1998.

[34] J. L. Keddie, R. A. L. Jones, and R. A. Cory. *Europhys. Lett.*, 27:59, 1994.

[35] G. Reiter. *Macromol.*, 27:3046, 1994.

[36] J. A. Forrest, K. Dalnoki-Veress, J. R. Stevens, and J. R. Dutcher. *Phys. Rev. Lett.*, 77:2002, 1996.

[37] T. Kajiyama, K. Tanaka, and A. Takahara. *Macromol.*, 30:280, 1997.

[38] J. A. Forrest, K. Dalnoki-Veress, and J. R. Dutcher. *Phys. Rev. E*, 56:5705, 1997.

[39] G. B. DeMaggio, W. E. Frieze, D. W. Gidley, M. Zhu, H. A. Hristov, and A. F. Yee. *Phys. Rev. Lett.*, 78:1524, 1997.

[40] S. Kawana and R. A. L. Jones. Character of the glass transition in thin supported polymer £lms. *Phys. Rev. E*, 63:021501, 2001.

[41] J. S. Huang and W. W. Webb. *Phys. Rev. Lett.*, 23:160, 1969.

[42] H. J. Kim, A. Ruehm, L. B. Lurio, J. Basu, J. Lal, D. Lumma, S. G. J. Mochrie, and S. K. Sinha. Surface dynamics of polymer £lms. *Phys. Rev. Lett.*, 90:1212, 2003.

[43] S. K. Sinha, E. B. Sirota, S. Garoff, and H. B. Stanley. X-ray and neutron scattering from rough surfaces. *Phys. Rev. B*, 38:2297, 1988.

[44] A. Braslau, M. Deutsch, P. S. Pershan, A. H. Weiss, J. Als-Nielsen, and J. Bohr. *Phys. Rev. Lett.*, 54:114, 1985.

[45] S. K. Sinha, E. B. Sirota, S. Garoff, and H. B. Stanley. *Phys. Rev. B*, 38:2297, 1988.

[46] C. Fradin, A. Braslau, D. Luzet, D. Smilgies, M. Alba, N. Boudet, K. Mecke, and J. Daillant. *Nature*, 403:871, 2000.

[47] J. Brandrup and E. H. Immergut, editors. *Polymer Handbook*. Wiley, New York, 1989.

[48] J. Wang, M. J. Bedzyk, and M. Caffrey. Resonance enhanced x-rays in thin £lms: A structure probe for membranes and surface layers. *Science*, 258:775–779, 1992.

[49] L. B. Lurio, A. Rühm, H. Kim, J. Lal, J. K. Basu, S. K. Sinha, and S. G. J. Mochrie. *unpublished*.

[50] D. J. Plazek and V. M. O'Rourke. *J. Poly. Sci.*, 9:209, 1971.

[51] M. W. Matsen. The stadard gaussian model for block copolymer melts. *J. Phys.: Condensed Matter*, 14:R21–R47, 2002.

[52] D. Roux, C. Coulon, and M. E. Cates. Sponge phases in surfactant solutions. *J. Phys. Chem.*, 96:4174–4187, 1992.

[53] G. Gompper and M. Schick. *Self-Assembling Amphiphilic Systems*. Academic Press, New York, 1994.

[54] S. A. Safran. *Statistical Thermodynamics of Surfaces, Interfaces, and Membranes*. Addison Wesley, New York, 1994.

[55] G. Gompper and M. Kraus. Ginzburg-landau theory of ternary amphiphilic systems: Monte carlo simulations. *Phys. Rev. E*, 47:4301, 1993.

[56] G. Gompper and M. Schick. Scattering from internal interfaces in microemulsion and sponge phases. *Phys. Rev. E*, 49:1478, 1994.

[57] M. Hennes and G. Gompper. Dynamical behavior of microemulsion and sponge phases in thermal equilibrium. *Phys. Rev. E*, 54:3811, 1996.

[58] A. G. Zilman and R. Granek. Undulations and dynamic structure factor of membranes. *Phys. Rev. Lett.*, 77:4788, 1996.

[59] M. Mihailescu, M. Monkenbusch, H. Endo, J. Allgaier, G. Gompper, J. Stellbrink, D. Richter, B. Jakobs, T. Sottmann, and B. Farago. Dynamics of bicontinuous microemulsion phases with and without amphiphilic block-copolymers. *J. Chem. Phys.*, 115:9563, 2001.

[60] M. Maugey and A. M. Bellocq. Effect of adsorbed and anchored polymers on membrane ¤exibility: A light scattering study of sponge phases. *Langmuir*, 17:6740, 2001.